PAPER • **OPEN ACCESS**

Characterisation of the interplay between microstructure and opto-electronic properties of $Cu(In,Ga)S_2$ solar cells by using correlative CL-EBSD measurements

To cite this article: Yucheng Hu *et al* 2024 *Nanotechnology* **35** 295702

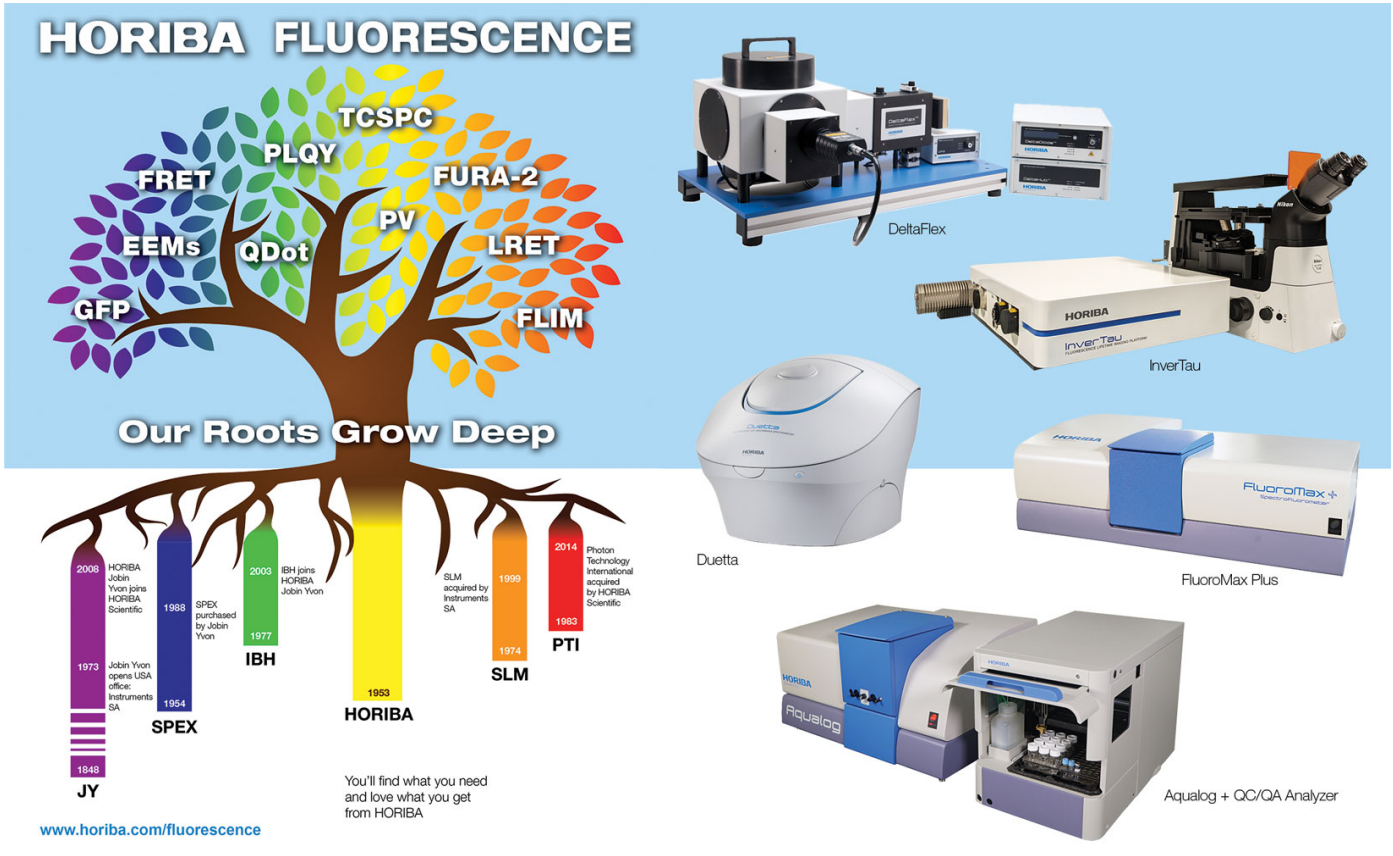

OPEN ACCESS
IOP Publishing
Nanotechnology

Nanotechnology **35** (2024) 295702 (10pp)
https://doi.org/10.1088/1361-6528/ad3bbd

Characterisation of the interplay between microstructure and opto-electronic properties of $Cu(In,Ga)S_2$ solar cells by using correlative CL-EBSD measurements

Yucheng Hu[1], Gunnar Kusch[1], Damilola Adeleye[2], Susanne Siebentritt[2] and Rachel Oliver[1]

[1] Department of Materials Science and Metallurgy, Cambridge University, Cambridge CB3 0FS, United Kingdom
[2] Laboratory for Photovoltaics, Department of Physics and Materials Science Research Unit, University of Luxembourg, 44 Rue du Brill, 4422 Belvaux, Luxembourg

E-mail: yh478@cam.ac.uk

Received 17 October 2023, revised 22 March 2024
Accepted for publication 8 April 2024
Published 30 April 2024

Abstract

Cathodoluminescence and electron backscatter diffraction have been applied to exactly the same grain boundaries (GBs) in a $Cu(In,Ga)S_2$ solar absorber in order to investigate the influence of microstructure on the radiative recombination behaviour at the GBs. Two different types of GB with different microstructure were analysed in detail: random high angle grain boundaries (RHAGBs) and $\Sigma 3$ GBs. We found that the radiative recombination at all RHAGBs was inhibited to some extent, whereas at $\Sigma 3$ GBs three different observations were made: unchanged, hindered, or promoted radiative recombination. These distinct behaviours may be linked to atomic-scale grain boundary structural differences. The majority of GBs also exhibited a small spectral shift of about ± 10 meV relative to the local grain interior (GI) and a few of them showed spectral shifts of up to ± 40 meV. Red and blue shifts were observed with roughly equal frequency.

Supplementary material for this article is available online

Keywords: cathodoluminescence, electron backscatter diffraction, chalcopyrite, grain boundary, solar cells

1. Introduction

As a renewable and clean energy source, solar energy has received significant interest from society for many years. The photovoltaics market is dominated by crystalline Si solar cells, which have improved so strongly over recent years, that they are approaching their theoretical limits [1].

In order to further improve the solar cell efficiency, tandem solar cells, in which Si solar cells are part of a stack with another wide bandgap semiconductor on the top represent a good strategy [1]. Such a multi-junction structure allows the solar cell to break the Shockley–Queisser limit for Si, with theoretical efficiencies up to 45% [2]. Among the various available materials, chalcopyrite semiconductors have drawn much attention because they have a wide and tunable bandgap ranging from 1.0 to 2.4 eV [3]. The wide bandgap sulphide compounds are suitable for the absorption of short wavelength light. The electronic properties and excellent stability make wide gap chalcopyrite interesting for application as the top cell in Si-based tandem solar cells. Sulphide chalcopyrite, $Cu(In,Ga)S_2$ (CIGS), with a bandgap suitable for top cells in tandem applications has achieved efficiencies above 15% [4, 5], whereas the low bandgap selenide, $Cu(In,Ga)Se_2$ (CIGSe),

reaches efficiencies above 23%[6]. A major difference between the two types of devices is the open circuit voltage deficit, which is considerably higher in the sulphide devices than in the selenides [3]. Open circuit voltage losses in sulphides have been attributed to deep defects [5] and to bandgap variation between grains [7]. In selenide solar cells, these limitations are absent or much weaker [8, 9]. One may expect that with more development work these limitations can also be removed in sulphide solar cells. It has been proposed that state of the art selenide solar cells are limited by grain boundary recombination [10]. It is therefore also important to understand the properties of grain boundaries in sulphide absorbers.

According to the coincidence site lattice (CSL) theory, the structure of GBs can be described by the finite fraction of lattice sites that coincide between two adjacent lattices [11]. For convenience, the GBs in chalcopyrite are normally categorised into two types, $\Sigma 3$ GBs and random high angle grain boundaries (RHAGBs) [12]. $\Sigma 3$ GBs are low energy GBs, which can be described as twins. In the tetragonal chalcopyrite lattice, the $\Sigma 3$ GBs have a $\{112\}$ grain boundary plane with a $\langle 221 \rangle$ rotation axis. All GBs with Σ value larger than 3 are classified as RHAGBs. The structural difference between $\Sigma 3$ GBs and RHAGBs may lead to a change in the local band structure, influencing absorber opto-electronic behaviours and overall performance of the solar cell [12].

Several previous studies have reported the properties of GBs in the chalcopyrite material system. For example, Abou-Ras *et al* studied pure selenide chalcopyrite solar cells using cathodoluminescence (CL) and found that all investigated RHAGBs are detrimental to radiative recombination rate while $\Sigma 3$ GBs were found to have little or even no effect on the radiative recombination rate [13]. Müller *et al* observed that random GBs in CIGSe exhibit a redshift in CL emission energy, whereas the emission wavelength at $\Sigma 3$ GBs is shown no shift [12]. Shifts may indicate compositional or strain variation at the GB [12]. GBs in chalcopyrite materials have not so far been extensively studied in plan view, which can provide better statistics on the GB behaviour. Moreover, these studies usually focus on selenium-based chalcopyrite CIGSe, whereas its analogue, sulphur-based CIGS, has been little researched.

In this work, we focus on the direct correlation of the opto-electronic and structural properties of GBs in CIGS by CL and electron backscatter diffraction (EBSD) in plan view. Multi-microscopy characterisation—in which exactly the same area is studied in multiple different microscopy techniques—was applied in plan view on a CIGS absorber which had been carefully polished. The inter-relationship between radiative recombination activity and GB microstructure were investigated by analysing over 150 different GBs in directly correlated CL and EBSD maps.

2. Methods

The sample used in this study is a CIGS thin film absorber fabricated on a Mo-coated soda lime glass. The absorber was deposited by a 3-stage co-evaporation method under S-rich conditions, similar to absorbers reported in literature [5], with two important differences: the first stage temperature is higher and the Ga flux in first and third stage is not the same. The first and second/third stage substrate temperature are 435 °C and 590 °C, respectively. These temperatures are deduced from the reading of a thermo couple near the heater and a measured calibration curve using a pyrometer. The In flux in first and third stage are the same, the Ga flux in third stage is lower than in first stage. The Cu/(Ga+In) atomic ratio of the resulting film is 0.95 and the overall Ga/(Ga+In) atomic ratio is 0.11, both are determined from energy dispersive x-ray spectroscopy (EDX), using an electron beam at 20 keV, and contain the usual EDX errors of a few % in atomic composition. Room temperature photoluminescence (PL) spectra show the maximum emission at 1.53 eV. The 3-stage process leads to a Ga profile and a bandgap profile, the PL maximum is expected to correspond to the bandgap minimum [14].

The as grown sample has a rough surface morphology (see supplementary information figure 1). Thus, the sample front surface was polished using a Gatan Ilion broad ion beam system, to prepare a smooth surface for EBSD measurement and to limit the influence of topography variation on the CL signal. The polishing was done by an Ar^+ beam with an energy of 4 kV at a temperature of 80 K for 45 min. The beam angle was 2° and the sample was slowly rotated during the polishing steps with a speed of 3 rotations per minute. The resulting surface has a bowl-like shape with a small circular area at the centre of the sample where the film has been entirely polished through. Six CL and EBSD maps were taken from different positions across the polished surface and the full dataset is illustrated in figure 2 in the supplementary information.

The opto-electronic properties of CIGS were measured by using an Attolight Allalin 4027 Chronos dedicated CL-SEM. All CL maps were acquired with 3 kV beam energy, 1.25 nA measurement current, and 50 μm aperture size. The typical dwell time per pixel was 0.5 s. Where specific maps used a different dwell time, this is indicated in the supplementary information. The estimated depth of the interaction volume is about 55 nm according to Monte Carlo simulations using the Monte Carlo CASINO software [15]. All measurements were performed at room temperature. The CL data analysis was performed using Lumispy, an open-sourced python library [16].

The microstructure of the CIGS sample was acquired by using a ZEISS GeminiSEM equipped with an Oxford Instrument HKL Symmetry S3 EBSD Detector and Oxford Instruments HKL AZtecHKL 4 software. The EBSD acceleration voltage is 15 kV. Most EBSD maps have approximately 5 μm x 5 μm area, with 30 nm step size for each pixel. The depth of the EBSD interaction volume under this voltage should be comparable to the CL interaction volume. For pattern indexing, the phase of the material is assumed to be zinc blende lattice with lattice parameter = 0.558 nm. The cubic lattice, rather than the tetragonal lattice, was used because the tetragonal CIGS has pseudo-symmetry, with c/a ratio too close to 2 [17]. With the presence of pseudo-symmetry, a few distinct phase orientations may have highly similar EBSD patterns, which are hard to distinguish by most EBSD indexing methods [18]. The application of cubic phase

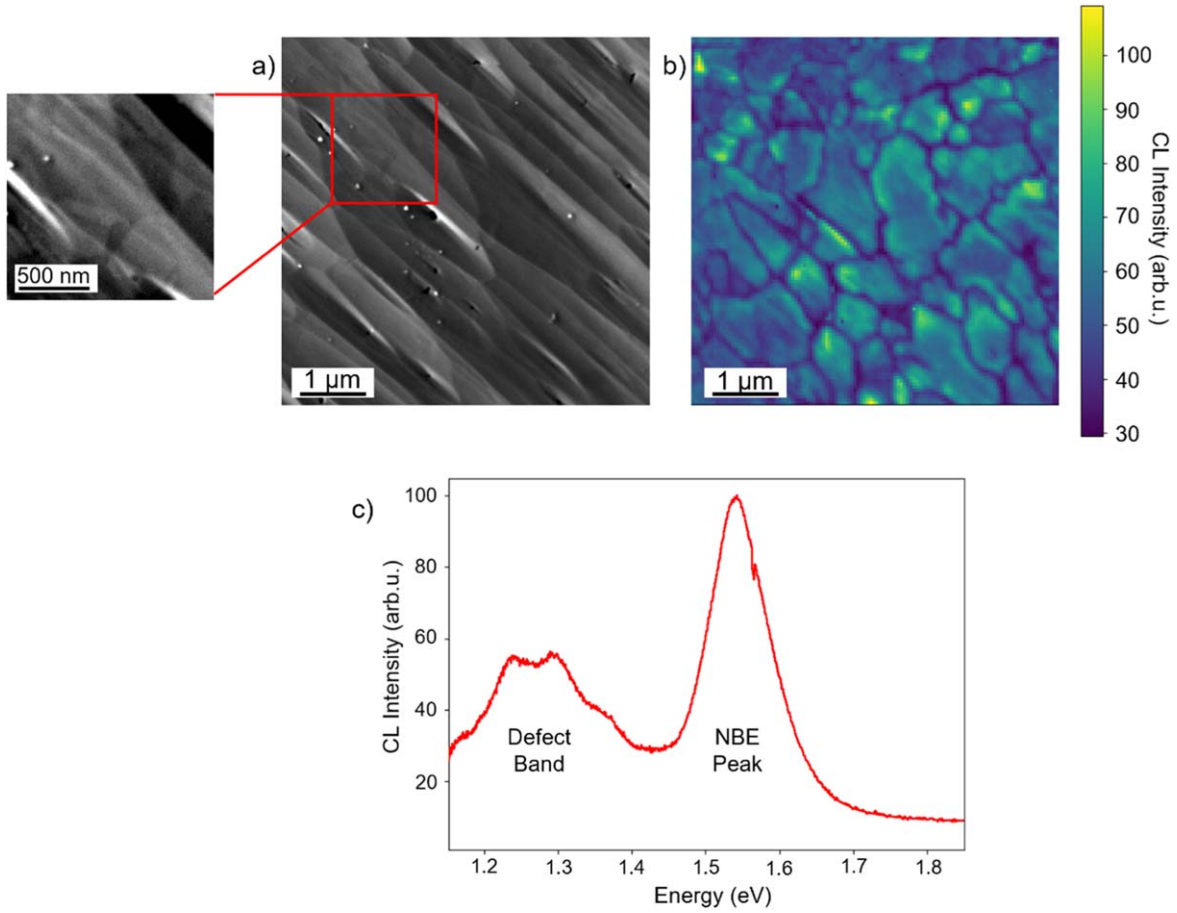

Figure 1. (a) SE image (Map 1), (b) panchromatic CL image from the same region and (c) CL mean spectrum of correlated Map 1. A small area of SE was cropped out and adjusted for a clear visualisation of grain structure patterns.

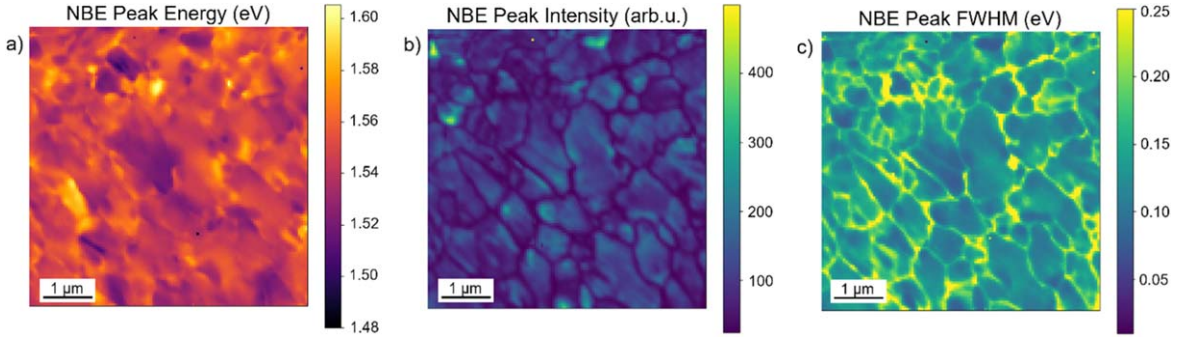

Figure 2. (a) NBE peak energy map, (b) NBE peak intensity map, and (c) NBE peak FWHM map.

indexing can avoid potential extensive EBSD mis-indexing and does not have significant influence on GB CSL analysis. The difference in GB computation results between cubic and tetragonal phase will be explained in more detail in the EBSD results section. The EBSD data was analysed using MTEX, an open-sourced MATLAB toolbox [19]. During the data analysis, indexed areas smaller than 5 pixels were removed from dataset, and all indexed areas larger than 5 pixels were identified as grains. Grains were reconstructed with a threshold angle, namely the misorientation angle between grain area and surrounding boundaries, of 5 degrees.

3. Results

3.1. Opto-electronic properties by CL

The SE image in figure 1(a) shows the surface morphology of the polished sample. An example SE image of an unpolished surface can be seen in supplementary information figure 1. After the Ar^+ ion beam polishing, the resulting sample has a much smoother surface with small edge- and groove-like features. Several randomly distributed small particles can also be observed on the SE image. These particles formed during the surface polishing step due to the preferential sputtering of Cu

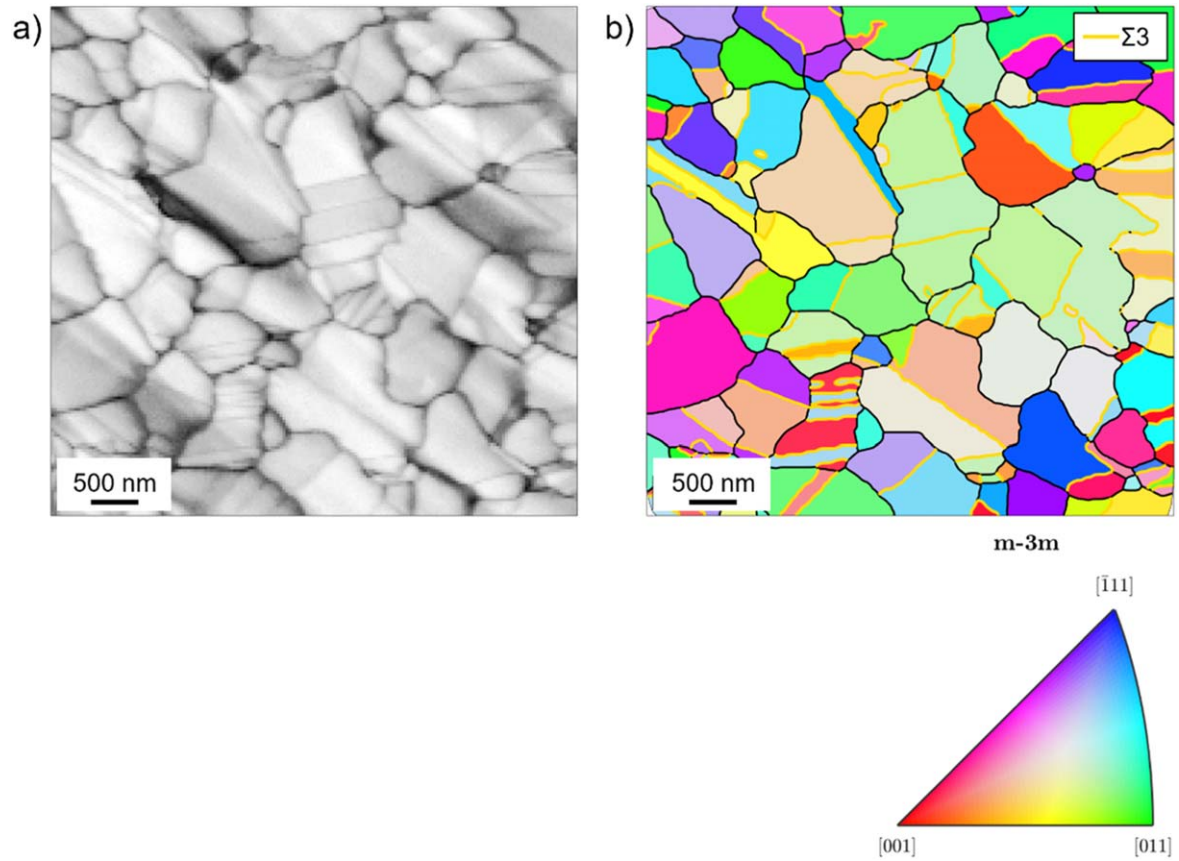

Figure 3. (a) EBSD band contrast (or pattern quality) image and (b) orientation map in which grain orientations are coloured according to the inverse pole figure colour key. Σ3 GBs are highlighted in (b) by yellow lines.

[20]. The size of Cu particles is usually quite small, with a radius well below 100 nm. These particles thus only affect the CL measurements on a highly localised area. The SE image also reveals weak contrast that may be indicative of the underlying grain structure. A small area of SE image with adjusted brightness and contrast was cropped for better visualisation of this structure and is shown alongside figure 1(a). Figure 1(b) is a panchromatic CL map from the same region, which highlights changes in recombination activity. Grain-like structures separated by dark boundaries are observed from the panchromatic CL. The CL intensity contrast between grain and boundary may be attributed to the high density of non-radiative recombination centres at typical GBs, such as point defects and dangling bonds [21]. Apart from the difference between GB and grain interior (GI), the CL intensity also shows noticeable fluctuations within grains, which may be attributed to variations in doping density and minority carrier lifetime [10]. figure 1(c) shows the mean CL spectrum, which contains a strong emission peak at 1.54 eV and a broad low intensity peak at 1.25–1.3 eV. We associate the former peak to near band edge (NBE) transitions, in agreement with the PL spectra, and the lower energy peak to a radiative defect-assisted recombination process. To be more specific, the NBE peak arises from the combination of several transitions with near-band-gap emission energy, such as band-to-band transitions, shallow donor-shallow acceptor pair transitions, and free carriers to donor or acceptor transitions. PL results acquired at low temperature suggest that a clearer fingerprint of the NBE recombination processes, such as the appearance of multiple donor–acceptor pairs, can be obtained when measuring at cryogenic temperatures [3, 22], possibly helping us to further distinguish between different recombination processes in our sample. The broad radiative defect-assisted recombination may be attributed to deep defect transitions.

The panchromatic CL image was extracted from the recorded hyperspectral dataset where each pixel contains a full CL emission spectrum. To distinguish the band-to-band recombination from the defect-assisted transition, we fit a Gaussian peak to both the NBE peak and the defect-related peak. The Gaussian fitting results, including peak emission energy, intensity, and full-width-half-maximum (FWHM) of the NBE peak, are shown in figure 2. Unlike the intensity and FWHM maps, the NBE emission energy map does not show a clear microstructure as there is no systematic energy difference between GI and GB. NBE emission energy non-uniformities with a standard deviation of 13 meV were observed. This is considerably lower bandgap fluctuation than reported in literature [7], indicating the higher quality of these newer absorbers. In terms of FWHM, most of the apparent GBs show a broadening of the CL peak relative to the GI which may be due to overlap in measurement of two adjacent grains with different emission energies. More analysis of the intensity and the NBE peak energy changes at the GBs will be presented in CL-EBSD correlative analysis section.

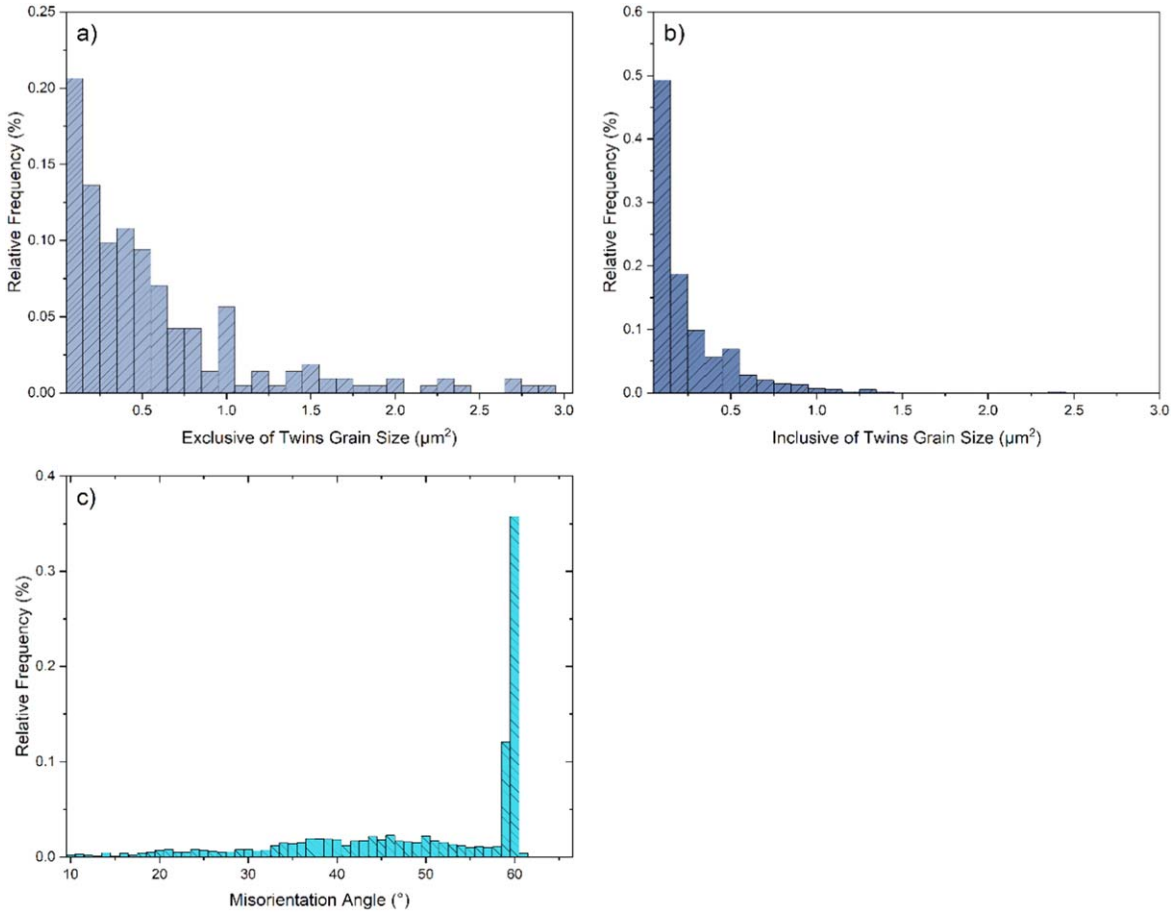

Figure 4. Histograms showing the statistics of (a) the CIGS ET grain size, and (b) the CIGS IT grain size, and (c) the GB misorientation angle as measured across 6 different EBSD maps.

3.2. Structural properties by EBSD

The EBSD band contrast map in figure 3(a) provides a clear visualisation of the sample microstructure. The imaging area of the EBSD map is exactly the same as that in figures 1 and 2. Figure 3(b) shows a map of the grain orientation, with the orientation of each grain indicated by its colour. The random distribution of colours, without any dominant shade, suggests that there is no preferential grain orientation. This observation is consistent across all measured areas. Σ3 GBs with 60° misorientation angle are indicated as in yellow.

The grain size distribution statistics are presented in figures 4(a) and (b). In this analysis, grain size was computed in two ways, counting the size of only the parent grain and counting the size of sub-grains within the same parent grain but separated by twin boundaries, according to the method proposed by Sahu *et al* [23]. We will refer to these two counting methods as grain size excluding twin boundaries (ET) counting and grain size including twin boundaries (IT) counting, respectively. The results show that nearly 70% of the IT grains are micro-grains with a grain size below 0.25 μm^2. In contrast, ET grains have a much larger variance, with an increase in the maximum grain size. The ratio between mean ET and mean IT grain size is 2.28, aligning with the high density of twin boundaries or Σ3 GBs the sample [24].

The histogram in figure 4(c) shows that 47.8% of all GBs have a misorientation angle of about 60°, which corresponds to the misorientation angle of Σ3 GBs. It is worth highlighting that the Σ3 GBs exhibited in the EBSD results stand for {111} GB planes with ⟨111⟩ rotation axis in cubic phase. These planes are equivalent to the actual Σ3 GB planes, the {112} GB planes with a ⟨221⟩ rotation axis, in the actual chalcopyrite tetragonal phase. The high relative frequency of Σ3 GBs may be explained by their twinning nature. Since twin boundaries typically contain nearly no dangling bonds, the formation energy of twin boundaries is relatively low, making the formation of twin boundaries preferred over the formation of RHAGBs in the material [25]. Similar GB statistics dominated by 60° Σ3 GBs have been reported in other studies with cubic phase EBSD indexing [25]. It should be noted that the GB misorientation angle statistics may be different in other research with tetragonal phase EBSD indexing, where Σ3 GBs at both ∼60° and ∼70° were observed as well [12, 26]. The difference in misorientation angle calculation may be attributed to the difference in EBSD indexing phase [17]. Some distinct tetragonal crystal planes may not be distinguished if the crystal system changes to cubic from tetragonal, and hence the calculation of misorientation angle will also be different.

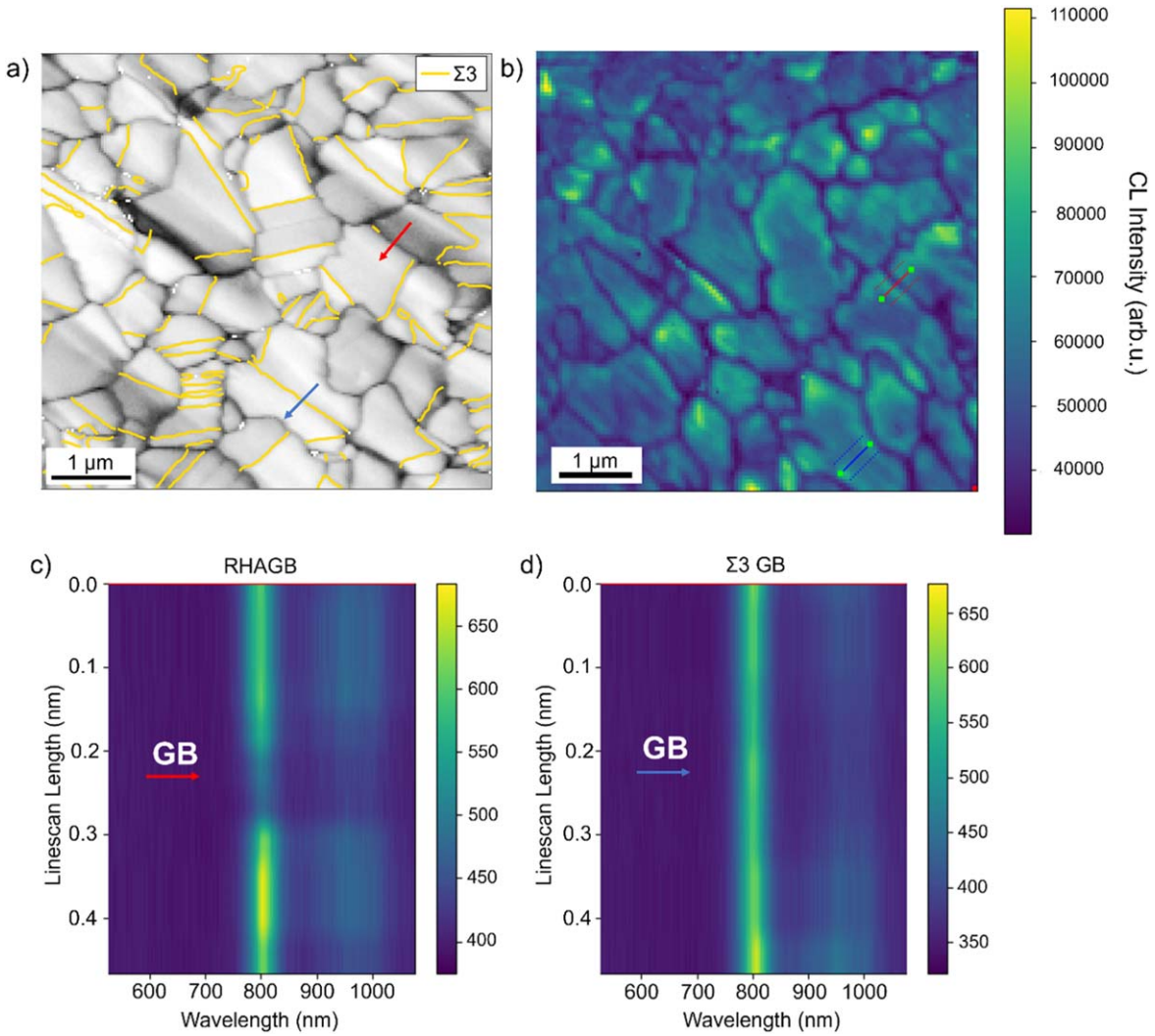

Figure 5. (a) EBSD band contrast diagram with highlighted Σ3 GBs and (b) CL panchromatic plot. Markers indicate the line spectra passed through a RHAGB (red) and a Σ3 GB (blue). (c) and (d) are line spectra extracted from the linescans.

3.3. CL-EBSD correlative analysis

The CL and EBSD maps were acquired on the same region of interest for direct correlation of opto-electronic and structural properties. The CL map in figure 1 and the EBSD map in figure 3 were compared for correlative analysis, as shown in figure 5. To analyse the change in CL intensity and wavelength at different types of GBs, two line spectra were extracted from the panchromatic CL image. Figure 5(a) is a line spectrum taken along a line passing through a RHAGB, indicated by a red arrow, while figure 5(b) is taken from a line passing through a Σ3 GB, indicated by a blue arrow. The line spectra revealed a significant reduction—of about 50%—in the intensity of the NBE emission at the RHAGB, whereas there was minimal change observed at the Σ3 GB. Similar trends were found for the defect-related emission. Additionally, no significant changes in the wavelength of the NBE were observed in this case at either the Σ3 GB or the RHAGB.

To increase the statistical robustness of our analysis, an additional 5 maps were taken from different areas of the sample surface using similar CL and EBSD characterisation settings. More line spectra were extracted, and the signal change at different GBs (ΔSignal) was quantified by the formula shown below

$$\Delta\text{Signal} = \frac{(\text{GI}\quad \text{Signal}_{\text{LHS}} + \text{GI}\quad \text{Signal}_{\text{RHS}})}{2} - \text{GB}\quad \text{Signal}.$$

The opto-electronic properties of the GI, such as CL intensity and emission energy, can vary substantially on the two sides of a GB as a result of differences in grain orientation and local defect density [7]. To minimise the impact of GI variation, we used the CL signal of the GI sitting at the lefthand side (GI $\text{Signal}_{\text{LHS}}$) and righthand side (GI $\text{Signal}_{\text{RHS}}$) of the GB to calculate the mean GI signal. All 6 correlated maps and the different linescan positions are shown in the supplementary information.

A total of 74 Σ3 GBs and 75 RHAGBs from 6 different maps were analysed to investigate the effect of the GB microstructure on the CL intensity, and the statistical results are shown in figure 6. The results show that a reduction in CL

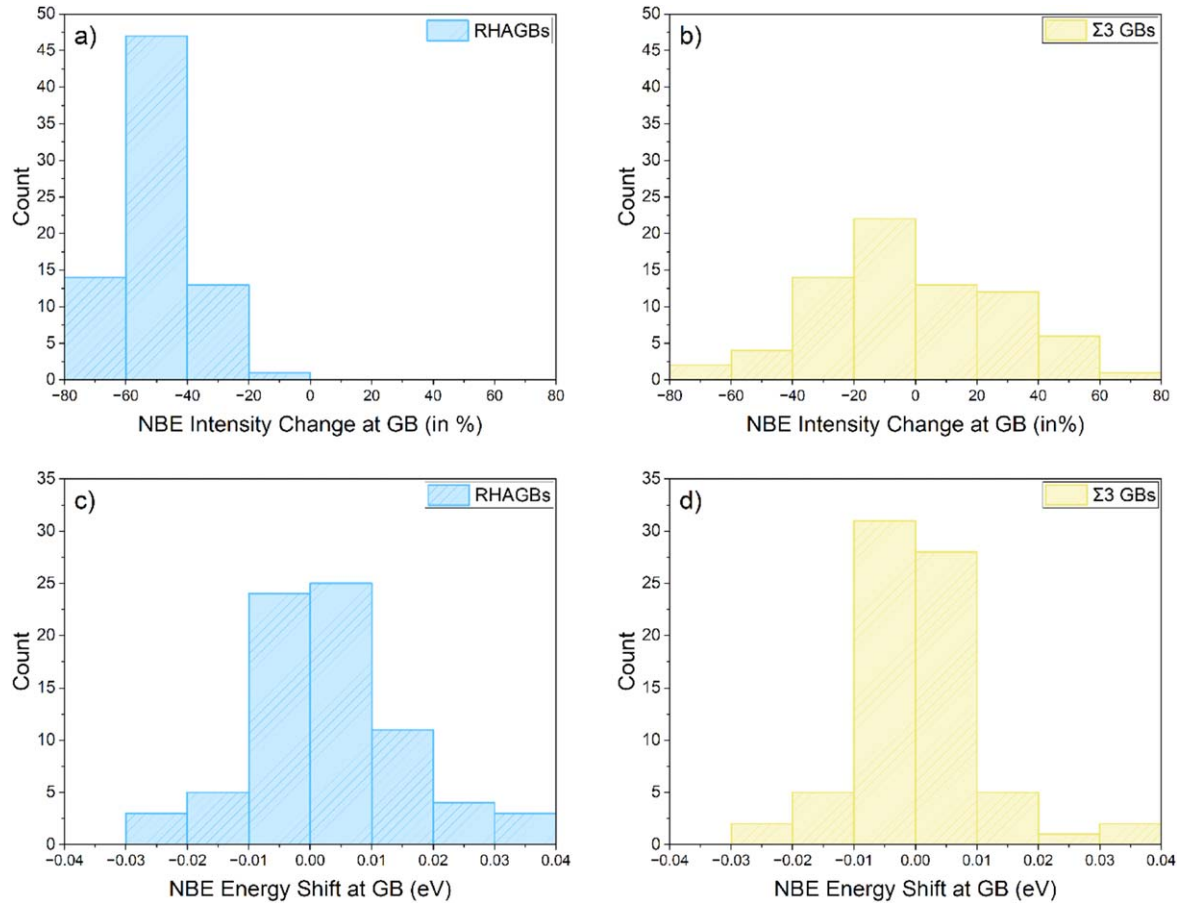

Figure 6. Histograms show the count versus relative NBE peak intensity change at (a) RHAGBs and (b) Σ3 GBs, and the count versus NBE peak emission energy shift at (c) RHAGBs and (d) Σ3 GBs.

intensity was observed at all RHAGBs, indicating a strong inhibition of radiative recombination.

The situation regarding Σ3 GBs is more complicated than that of RHAGBs. Out of the 74 Σ3 GBs analysed, approximately 47% were found to be opto-electronically neutral, exhibiting an intensity fluctuation of only ± 20%, similar to the example Σ3 GB line spectra shown in figure 5. Apart from the neutral Σ3 GBs, about half of the Σ3 GBs were found to have an impact on the CL intensity. As shown in figure 6, 27% of Σ3 GBs appear darker than adjacent GI with a CL intensity drop greater than 20% while 26% of Σ3 GBs shown an increase in the CL intensity. This implies that radiative recombination activity may be degraded or even promoted at some Σ3 GBs. The enhanced CL intensity at Σ3 GBs is an interesting observation which has not previously been reported in chalcopyrite-based films. Two examples of high CL intensity Σ3 GBs are highlighted by red arrows crossing the GBs in figure 7, and the corresponding linescans across these two bright Σ3 GBs are shown in figures 7(c) and (d), further illustrating the increased intensity in the GB region.

The NBE emission energy shifts at different grain boundaries were investigated and the data of 74 Σ3 GBs and 75 RHAGBs are shown in figures 6(c) and (d), respectively. Both Σ3 GBs and RHAGBs exhibit similar trend in terms of NBE emission energy shift, with an approximately equal proportion of blueshifts and redshifts. Most GBs show a weak shift below 15 meV, which is comparable to the standard deviation of the fitted NBE emission energy across the map (∼10–20 meV). Only 20% of Σ3 GBs and 35% of RHAGBs show strong emission energy change greater than 20 meV. Local element distribution and defect chemistry at GBs may influence the energy levels of shallow donors and/or acceptors and the bandgap, resulting in the observed redshifts and blueshifts of NBE transitions [3]. Previous studies in selenide chalcopyrite have reported the presence of Cu depletion or Cu enrichment at RHAGBs, leading to changes in local band structure and spectral shift [26, 27]. Our observation is quite distinct from the results reported by Abou-Ras *et al* [12] and Romero *et al* [28], where only 10–15 meV redshift were observed at RHAGBs in CIGSe. Several factors, including the sample deposition method, surface preparation method, and sample composition homogeneity, may contribute to the observation difference in spectral shift.

4. Discussion

Considering the high performance of over 15% conversion efficiency [5] of polycrystalline CIGS solar cells, there are two possible contributions to a reduced radiative recombination rate at the RHAGBs: (1) a higher density of defect states enhances

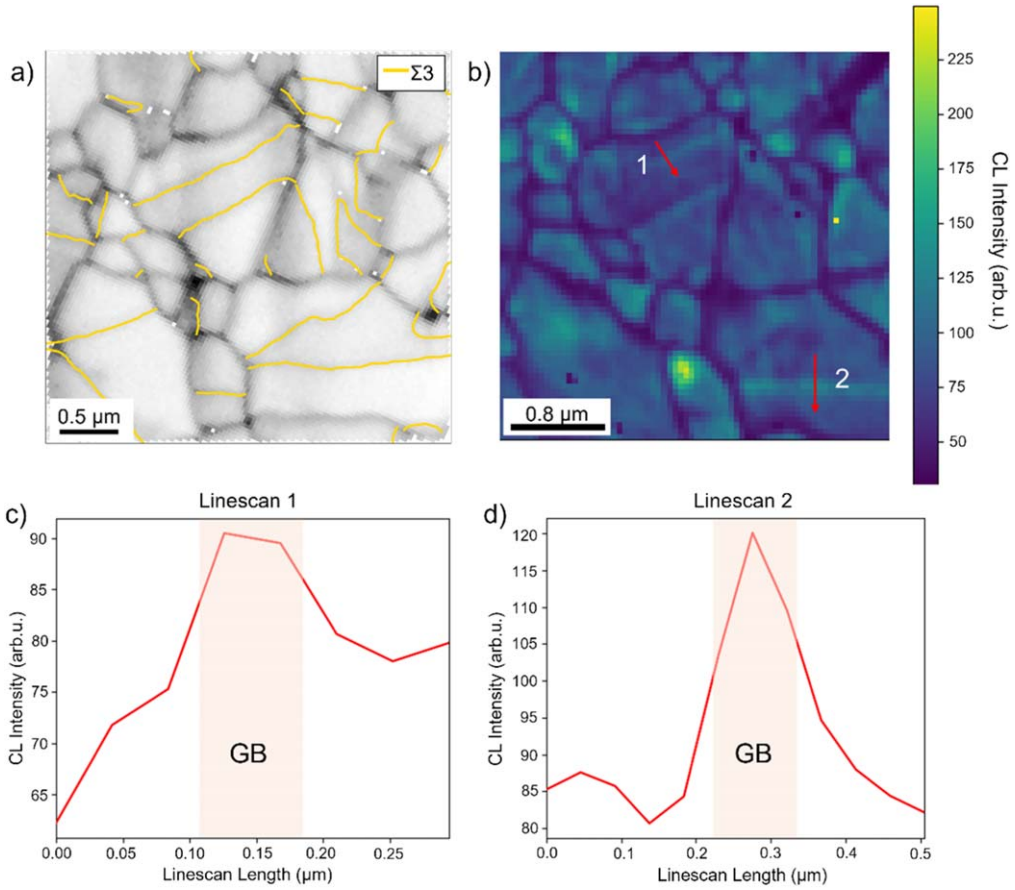

Figure 7. (a) EBSD map and (b) CL NBE intensity map of Map 6. The Σ3 GBs were highlighted with yellow lines in EBSD maps. Red arrows indicated 2 Σ3 GBs with enhanced CL intensity, and the corresponding extracted linescans were shown in (c) and (d).

competing non-radiative recombination; (2) local band bending leads to effective charge carrier separation. The first situation is commonly observed in most solar cell materials, such as Si [29], GaAs [30], and CIGSe [10]. For the second option, Raghuwanshi *et al* observed an enhanced electron beam induced current (EBIC) signal at some GBs in a correlative EBIC-EBSD measurements on CIGSe, which may indicate the separation of charge carriers at specific GBs [26].

The radiative recombination activity change at Σ3 GBs is more complicated. Three different explanations are proposed for different observations:

1. For opto-electronically neutral Σ3 GBs, the possible explanation may be associated with the twinning nature of Σ3 GBs. In an ideal Σ3 GB, both sides of the GB are highly symmetric and only differ in grain orientation. Consequently, Σ3 GBs should be virtually free of additional defects and have no or limited influence on carrier recombination.
2. The inhibition of radiative recombination at some Σ3 GBs may be explained by the presence of incoherent Σ3 GBs, which deviate slightly from the ideal twin boundary plane. The small angle deviation allows the presence and migration of point defects and dangling bonds at Σ3 GBs, potentially introducing non-radiative recombination sites or band bending similar to RHAGBs [31].
3. For Σ3 GBs with enhanced luminescence: Persson and Zunger in a first-principles calculation of model Σ3 GBs in $CuInSe_2$ and $CuGaSe_2$, reported a possible reduction in both the conduction and valence band energies (downward band bending) at metal cation-terminated Σ3 GBs in addition to a wider bandgap than adjacent the GI [32]. In addition, they noted an analogous upward band bending at Se-terminated Σ3 GBs [32]. Compared with downward bending, the upward bending had a much smaller energy change, leading to much weaker charge carrier confinement which may be relatively easy to overcome at room temperature. If CIGS GBs show similar electronic structure to CIGSe GBs, then the stronger downward band bending at cation-terminated GBs might provide an explanation of our results. Figure 8 illustrates a possible band edge profile structure at the bright Σ3 GBs, with downward band bending. Electrons are confined at a CB minimum. Whilst holes in this model experience a CB maximum at the same location, they may be localised adjacent to the GB via Coulomb attraction to the electrons. The Σ3 GB then acts effectively like a type II quantum well. The resulting carrier confinement may increase the radiative recombination rate and enhance the observed emission intensity [33]. If this explanation is correct, the CL at these bright Σ3 GBs should thus be red-shifted relative to the GI (as

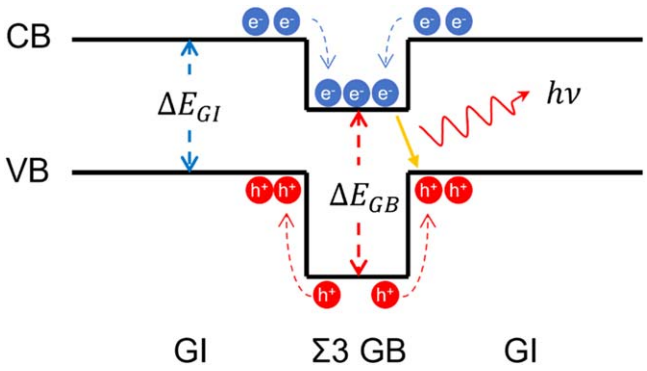

Figure 8. Schematic illustrates the possible bandgap change at narrow bright Σ3 GBs. The bandgap at Σ3 GBs (ΔE_{GB}) may be larger than that at GI (ΔE_{GI}), according to the calculation results in CIGSe [32]. The strong local band bending may act as a sink for electrons, and also repel holes. The electrons at the conduction band (CB) minimum of the Σ3 GB may recombine with the holes at the valence band (VB) maximum of adjacent GIs.

illustrated in figure 8) and may exhibit a narrower FWHM. By comparing the relative intensity change across all the Σ3 GBs with corresponding NBE energy change, a moderate negative correlation with a Pearson coefficient of −0.43 was found. The scatter plot illustrating the relationship between intensity change and the NBE energy change is shown in supplementary information figure 4. Nearly all Σ3 GBs that showed an increase in their emission intensity also show a slight redshift in their emission energy and a decrease in FWHM, both of which is compatible with the possibility that a quantum well-like structure is formed at the GB.

Although we are not aware of any reports of quantum well formation at twin boundaries in CIGS, there have been a few reports of quantum well behaviour at twin boundaries in cubic zinc blende materials, such as CdTe [34] and InP [35]. The presence of quantum well in those scenarios was attributed to the formation of heterostructure, in which a thin layer of hexagonal wurtzite phase at the twin boundary is embedded by two normal cubic zinc blende phase crystal [34]. Further investigation of the detailed crystal structure at CIGS twin boundaries, via TEM, may thus aid understand of the observed phenomenon.

5. Conclusion

In summary, CL and EBSD measurements were conducted on a polished CIGS absorber front surface in plan view to study and link the opto-electronic and structural properties. The CIGS absorber is polycrystalline with a high proportion of Σ3 GBs at 60° but without any observable preferred grain orientation. The CL intensity and NBE energy exhibited considerable variation within and across different grains. By correlating the CL and EBSD results of GBs, we investigated the influence of GB microstructure on the radiative recombination activity in CIGS. All RHAGBs strongly inhibited the radiative recombination, while Σ3 GBs were found with three different types of behaviour: about 45% of Σ3 GBs are neutral and the rest may either inhibit or promote radiative recombination in CL. Ideal twinning behaviour, incoherent Σ3 GBs and formation of local quantum well like features were suggested to be likely explanations of the various behaviours observed at Σ3 GBs. In terms of emission energy, most of the RHAGBs and Σ3 GBs showed only ±15 meV spectral shift but a small number of GBs exhibited spectral shifts of up to ±40 meV.

Acknowledgments

Cambridge authors would like to acknowledge funding from the EPSRC under EP/V029231/1 and EP/R025193/1. Luxembourg team would like to thank Luxembourgish Fond National de la Recherche (FNR) for funding in the framework of the MASSENA project (Project No. PRIDE 15/10935404), and the as well as the REACH (Project No. INTER/UKRI/20/15050982).

Data availability statement

The data that support the findings of this study are openly available at the following URL/DOI: https://doi.org/10.17863/CAM.102000 [36].

Conflict of interest

The authors have no conflicts of interest to disclose.

ORCID iDs

Yucheng Hu https://orcid.org/0009-0008-0888-0299
Gunnar Kusch https://orcid.org/0000-0003-2743-1022
Damilola Adeleye https://orcid.org/0000-0001-6359-9100
Susanne Siebentritt https://orcid.org/0000-0001-6522-1427
Rachel Oliver https://orcid.org/0000-0003-0029-3993

References

[1] Hermle M, Feldmann F, Bivour M, Goldschmidt J C and Glunz S W 2020 Passivating contacts and tandem concepts: approaches for the highest silicon-based solar cell efficiencies *Appl. Phys. Rev.* **7** 021305
[2] Eperon G E, Hörantner M T and Snaith H J 2017 Metal halide perovskite tandem and multiple-junction photovoltaics *Nat. Rev. Chem.* **1** 0095
[3] Siebentritt S, Lomuscio A, Adeleye D, Sood M and Dwivedi A 2022 Sulfide chalcopyrite solar cells—Are they the same as selenides with a wider bandgap? *Phys. Status Solidi—Rapid Res. Lett.* **16** 2200126

[4] Barreau N *et al* 2022 Investigation of co-evaporated polycrystalline Cu(In,Ga)S_2 thin film yielding 16.0% efficiency solar cell *EPJ Photovolt.* **13** 17

[5] Shukla S *et al* 2021 Over 15% efficient wide-band-gap Cu(In,Ga)S_2 solar cell: suppressing bulk and interface recombination through composition engineering *Joule* **5** 1816–31

[6] Green M A *et al* 2023 Solar cell efficiency tables (version 62) *Prog. Photovolt. Res. Appl.* **31** 651–63

[7] Sean P *et al* 2023 Role of nanoscale compositional inhomogeneities in limiting the open circuit voltage in Cu(In,Ga)S_2 solar cells *APL Energy* **1** 026104

[8] Gütay L, Lienau C and Bauer G H 2010 Subgrain size inhomogeneities in the luminescence spectra of thin film chalcopyrites *Appl. Phys. Lett.* **97** 052110

[9] Werner F *et al* 2018 Alkali treatments of Cu(In,Ga)Se_2 thin-film absorbers and their impact on transport barriers *Prog. Photovolt. Res. Appl.* **26** 911–23

[10] Krause M *et al* 2020 Microscopic origins of performance losses in highly efficient Cu(In,Ga)Se_2 thin-film solar cells *Nat. Commun.* **11** 4189

[11] Humphreys J, Rohrer G S and Rollett A 2017 Chapter 4—the structure and energy of grain boundaries *Recrystallization and Related Annealing Phenomena* ed J Humphreys, G S Rohrer and A Rollett (Elsevier) 3rd edn pp 109–43

[12] Müller M, Abou-Ras D, Rissom T, Bertram F and Christen J 2014 Symmetry dependent optoelectronic properties of grain boundaries in polycrystalline Cu(In,Ga)Se_2 thin films *J. Appl. Phys.* **115** 023514

[13] Abou-Ras D *et al* 2013 Electron backscatter diffraction: an important tool for analyses of structure-property relationships in thin-film solar cells *JOM* **65** 1222–8

[14] Wolter M H *et al* 2018 Influence of sodium and rubidium postdeposition treatment on the quasi-fermi level splitting of Cu(In,Ga)Se_2 thin films *IEEE J. Photovolt.* **8** 1320–5

[15] Drouin D *et al* 2007 CASINO V2.42—a fast and easy-to-use modeling tool for scanning electron microscopy and microanalysis users *Scanning* **29** 92–101

[16] Lähnemann J *et al* (2023) *LumiSpy/lumispy: v0.2.2 (v0.2.2).* (https://doi.org/10.5281/zenodo.7747350)

[17] Abou-Ras D, Schorr S and Schock H W 2007 Grain-size distributions and grain boundaries of chalcopyrite-type thin films *J. Appl. Crystallogr.* **40** 841–8

[18] Pang E L, Larsen P M and Schuh C A 2020 Resolving pseudosymmetry in tetragonal ZrO_2 using electron backscatter diffraction with a modified dictionary indexing approach *J. Appl. Crystallogr.* **53** 1060–72

[19] Niessen F, Nyyssönen T, Gazder A A and Hielscher R 2022 Parent grain reconstruction from partially or fully transformed microstructures in MTEX *J. Appl. Crystallogr.* **55** 180–94

[20] Abou-Ras D *et al* 2012 Enhancements in specimen preparation of Cu(In,Ga)(S,$Se)_2$ thin films *Micron* **43** 470–4

[21] Yacobi B G and Holt D B 1986 Cathodoluminescence scanning electron microscopy of semiconductors *J. Appl. Phys.* **59** R1–24

[22] Spindler C *et al* 2019 Electronic defects in Cu(In,Ga)Se_2: towards a comprehensive model *Phys. Rev. Mater.* **3** 090302

[23] Sahu S, Yadav P C and Shekhar S 2018 Use of hot rolling for generating low deviation twins and a disconnected random boundary network in inconel 600 alloy *Metall. Mater. Trans. A* **49** 628–43

[24] Field D P, Bradford L T, Nowell M M and Lillo T M 2007 The role of annealing twins during recrystallization of Cu *Acta Mater.* **55** 4233–41

[25] Abou-Ras D *et al* 2016 Grain-boundary character distribution and correlations with electrical and optoelectronic properties of $CuInSe_2$ thin films *Acta Mater.* **118** 244–52

[26] Raghuwanshi M *et al* 2018 Evidence of enhanced carrier collection in Cu(In,Ga)Se_2 grain boundaries: correlation with microstructure *ACS Appl. Mater. Interfaces* **10** 14759–66

[27] Kim K *et al* 2022 Atom-scale chemistry in chalcopyrite-based photovoltaic materials visualized by atom probe tomography *ACS Appl. Mater. Interfaces* **14** 52825–37

[28] Romero M J *et al* 2003 Cathodoluminescence of Cu(In,Ga)Se_2 thin films used in high-efficiency solar cells *Appl. Phys. Lett.* **83** 4770–2

[29] Fehr M *et al* 2012 Influence of deep defects on device performance of thin-film polycrystalline silicon solar cells *Appl. Phys. Lett.* **101** 123904

[30] Pouladi S *et al* 2019 Effects of grain boundaries on conversion efficiencies of single-crystal-like GaAs thin-film solar cells on flexible metal tapes *Sol. Energy Mater. Sol. Cells* **199** 122–8

[31] Schwarz T *et al* 2018 Correlative transmission Kikuchi diffraction and atom probe tomography study of Cu(In,Ga)Se_2 grain boundaries *Prog. Photovolt. Res. Appl.* **26** 196–204

[32] Persson C and Zunger A 2005 Compositionally induced valence-band offset at the grain boundary of polycrystalline chalcopyrites creates a hole barrier *Appl. Phys. Lett.* **87** 1–3

[33] Chichibu S, Wada K and Nakamura S 1997 Spatially resolved cathodoluminescence spectra of InGaN quantum wells *Appl. Phys. Lett.* **71** 2346–8

[34] Sun C *et al* 2013 Creating a single twin boundary between two CdTe (111) wafers with controlled rotation angle by wafer bonding *Appl. Phys. Lett.* **103** 252104

[35] Jiming B *et al* 2008 Optical properties of rotationally twinned InP nanowire heterostructures *Nano Lett.* **8** 836–41

[36] Hu Y, Kusch G, Adeleye D, Siebentritt S and Oliver R 2024 Research Data Supporting 'Characterisation of the interplay between microstructure and opto-electronic properties of Cu(In,Ga)S2 solar cells by using correlative CL-EBSD measurements'. *Apollo — University of Cambridge Repository* (https://doi.org/10.17863/CAM.102000)